Tuning Ion Transport at the Anode-Electrolyte Interface *via* a Sulfonate-Rich Ion-Exchange Layer for Durable Zinc-Iodine Batteries

Leiqian Zhang, Jiajia Huang, Hele Guo, Lingfeng Ge, Zhihong Tian, Mingjie Zhang, Jingtao Wang, Guanjie He, Tianxi Liu, Johan Hofkens, Dan J.L. Brett, and Feili Lai**

L. Zhang, Prof. J. Huang, M. Zhang, Prof. J. Wang
School of Chemical Engineering, Zhengzhou University, Zhengzhou 450001, P. R. China
E-mail: huangjiajia@zzu.edu.cn

H. Guo, Prof. J. Hofkens, Dr. F. Lai
Department of Chemistry, KU Leuven, Celestijnenlaan 200F, Leuven 3001, Belgium
E-mail: feili.lai@kuleuven.be

L. Ge
School of Chemistry, University of Bristol, Cantock's Close, Bristol, BS8 1TS, UK

Prof. Z, Tian
Engineering Research Center for Nanomaterials, Henan University, Kaifeng 475004, P. R. China

Prof. G. He, Prof. D. J.L. Brett
Electrochemical Innovation Lab, Department of Chemical Engineering, University College London, London, WC1E 7JE, UK

Prof. T. Liu
Key Laboratory of Synthetic and Biological Colloids, Ministry of Education, School of Chemical and Material Engineering, Jiangnan University, Wuxi 214122, P. R. China

Prof. J. Hofkens, Dr. F. Lai
Department of Molecular Spectroscopy, Max Planck Institute for Polymer Research, Ackermannweg 10, Mainz 55128, Germany

Abstract

Rechargeable aqueous zinc-iodine batteries (ZIBs) are considered a promising newly-developing energy-storage system, but the corrosion and dendritic growth occurring on the anode seriously hinder their future application. Here, the corrosion mechanism of polyiodide is revealed in detail, showing that it can spontaneously react with zinc and cause rapid battery failure. To address this issue, a sulfonate-rich ion-exchange layer (SC-PSS) is purposely constructed to modulate the transport and reaction chemistry of polyiodide and Zn^{2+} at the zinc/electrolyte interface. The resulting ZIBs can work properly over 6000 cycles with high-capacity retention (90.2%) and reversibility (99.89%). Theoretical calculations and experimental characterization reveal that the SC-PPS layer blocks polyiodide permeation through electrostatic repulsion, while facilitating desolvation of $Zn(H_2O)_6^{2+}$ and restricting undesirable two-dimension diffusion of Zn^{2+} by chemisorption.

1. Introduction

As one of the most promising electrical energy storage (EES) systems, lithium-ion batteries (LIBs) have dominated the energy-storage landscape for over 30 years.[1-3] In the pursuit of safety, cost-efficient, and green battery system today, however, LIBs are not capable of meeting these real requirements due to two fatal failures from the intrinsically inflammable organic electrolytes and the severe scarceness of lithium supplies.[2,4-6] Therefore, a lot of research efforts have been devoted to developing alternative energy storage technologies, complementary to LIBs, leading to the emergence of rechargeable aqueous zinc-iodine batteries (ZIBs) as a green and safe EES; this can be attributed to their intrinsic fire-retardant properties, richness in natural resources (0.0075% Zn in the earth crust and 55 $\mu g_{iodine} L_{ocean}^{-1}$), and the high energy (power) density of 750 Wh kg^{-1} (109.1 kW kg^{-1}).[7-10] Particularly, in consideration the redox couple of I_2/I^- in the cathode, ZIBs are able to present a flat

charge-recharge platform at 1.38 V that shows an unparalleled advantage over the counterparts with intercalation/de-intercalation mechanisms.[11,12] Nonetheless, ZIBs are encountering inadequate cycle life caused by the severe dissolution/diffusion of water-soluble polyiodide intermediates in electrolytes as well as the poor stability of the Zn anode.[13-15]

Some progress has been already made in obtaining better cathode materials in terms of suppressing the shuttle effect of polyiodide, including two-dimensional (2D) MXenes,[12] carbon-based materials,[16] Prussian blue analogues,[10] and organic materials.[17] Regardless of this, the performance and lifespan of the battery also depend heavily on the stability of the anode, especially in terms of achieving high durability.[18,19] Typically, in ZIBs, polyiodide escaping from the cathode during cycling will adversely affect the Zn anode with significant corrosion and passivation.[7] The corroded or passivated Zn anode will generate an uneven plating/stripping surface and exacerbate the Zn dendritic growth in aqueous electrolytes during cycling, which can pierce the separator and cause cell short circuit.[2,20] Thus, viable ZIBs are enabled only if the zinc anode is free of corrosion and passivation caused by the side reaction of polyiodide and water while maintaining dendrite-free deposition. Although bespoke considerations have huge impact on the applicability of ZIBs, they are often overlooked and urgently need to be understood and addressed.

Theoretically, ion transport (e.g., Zn^{2+} and I_3^-) occurs through the solid-liquid interface formed by the the metal anode and liquid electrolyte.[21,22] Therefore, it should be possible to control the interface chemistry to regulate Zn deposition behavior as well as the shuttle effect of polyiodide by constructing multifunctional protective layers on the Zn surface. For instance, Yang et.al sought assistance from a metal-organic framework layer to sieve iodine species and alleviate related parasitic side reactions on the Zn anode.[7] Adhering to the pursuit of low-cost, green, and large-scale EES, we have further found a famous and well-established technology, namely ion-exchange technology, which has been widely used in various fields, such as water

treatment,[23] energy storage,[24] and catalysis.[25] Typically, organic ion-exchange materials are composed of insoluble polymer skeleton and active groups, which are used to prevent the material from dissolving in water and determine the essential sorption characteristics of the material, respectively. Depending on the active group in the polymer skeleton, ion-exchange materials can therefore realize the enrichment and separation of various ions in water.[26] Inspired by this mechanism, we reasoned that by applying an ion-exchange layer, it would be possible to regulate Zn interfacial ion/molecule transport and to achieve excellent Zn plating/stripping behavior in ZIBs. Besides, ion-exchange fibers may be able to broaden the application of ZIBs in fiber batteries and flexible devices, as they can be utilized in various forms (e.g., filament, fabric, nonwoven, and felt). To be noted, the free water in the aqueous electrolyte will also attack the Zn anode during the cycling process and result in its rapid passivation and corrosion. Therefore, this protective barrier is also required to have inherent water-resistant properties, shielding the Zn anode from related parasitic side reactions.

Herein, we reveal the corrosion mechanism of polyiodide on the Zn anode, confirming that polyiodide can spontaneously react with Zn to form a thick and loose passivation layer on the Zn surface, which dramatically promotes dendrite growth and ultimately causes rapid battery failure. Therefore, a multifunctional sulfonated 1,4-bis(chloromethyl)-2-nitrobenzene crosslinked polyphenylene sulfide (noted as SC-PPS) coating is first constructed by employing the commercial polyphenylene sulfide fiber as the polymer skeleton and the sulfonic group as the active group to address the multiple issues, including polyiodide/water parasitic reactions and dendrites growth. As a result, the SC-PPS coating layer shows a high blockage effect toward polyiodide due to the electrostatic barrier formed by the rich sulfonic acid groups in SC-PPS, which effectively avoids the polyiodide corrosion towards the Zn anode. Meanwhile, Zn^{2+} is uniformly concentrated on the SC-PPS layer through chemical adsorption produced by the sulfonate-rich layer, which enables rapid 3D diffusion of Zn^{2+} at

the nucleation interface while facilitating the desolvation of $Zn(H_2O)_6^{2+}$ and reducing the free water to contact fresh Zn, thereby realizing highly reversible Zn plating/stripping. Befitting from bespoke effects, ZIBs with the SC-PPS coating can achieve an ultralong lifespan (>6000 cycles), as well as ultrahigh capacity retention (90.2%) and Coulombic efficiency (average of CE: 99.89%) at a high density of 3.2 A g^{-1}.
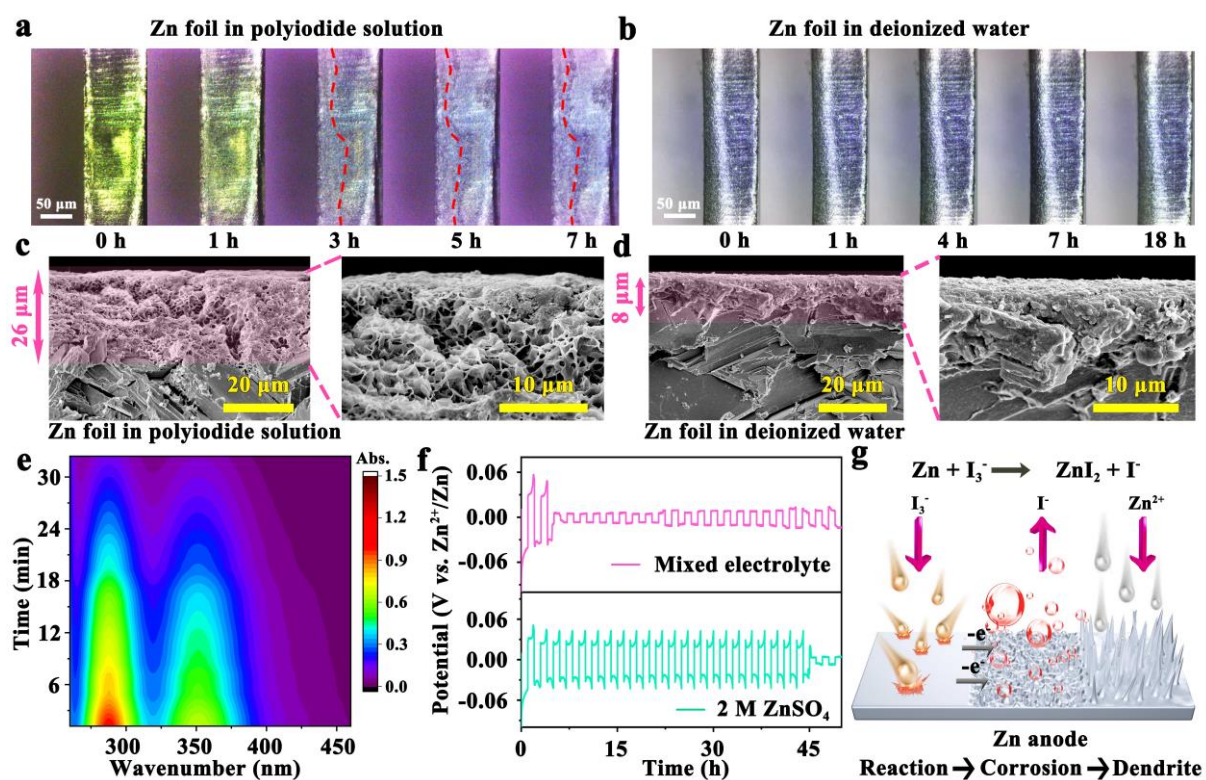
2. Results and Discussion

Figure 1. Corrosion processes of Zn foil in a) polyiodide solution and b) deionized water observed by in-situ optical microscope. Cross-sectional images of Zn foil after soaking in c) polyiodide solution and d) deionized water for 3 days. e) In-situ UV-vis spectroscopy for I_3^- ions in polyiodide solution with fresh Zn foil. f) Electrochemical cycling behavior of symmetric Zn cells with the mixed electrolyte and 2 M ZnSO$_4$ electrolyte at a current density of 1 mA cm^{-2} (1 mAh cm^{-2}). g) Schematic diagram for the mechanism of polyiodide corroding Zn anode.

Although Yang and co-workers have revealed that polyiodide can corrode Zn anode,[7] the understanding of underlying mechanisms remains obscure. Therefore, we deemed it necessary to improve and supplement the theoretical basis of polyiodide corrosion of zinc before carrying out follow-up works. Firstly, we investigated the corrosion behavior of the Zn foil in a polyiodide solution (composed of 1 M KI and 0.01 M I_2 in deionized water) by conducting in-situ optical microscope (OM). As shown in **Figure 1**a, the digital images clearly show the corrosion and passivation process on the Zn surface in a polyiodide solution, in which a bulge, formed on the Zn foil, is visually observed already after 5 h. By stark contrast, the Zn surface in deionized water presents a negligible change even after 18 h (Figure 1b). This observation confirms the accelerated corrosion effect of polyiodide on zinc foils. Furthermore, the cross-sectional morphologies of Zn foil in both solutions were further checked by scanning electron microscope (SEM) images (Figure 1c and 1d). The Zn foil in polyiodide solution suffers intense corrosion where the corrosion layer increases dramatically to ~26 μm. As compared with the shallow corrosion layer (~8 μm) in deionized water, it indicates that the corrosion of polyiodide has an inward tendency to jeopardize the stability of zinc anode seriously in an aqueous solution. Particularly, a by-no-means negligible phenomenon is that the corrosion layer in the polyiodide solution presents a honeycomb structure, while it is fully dense in deionized water. It is well-known that a dense protective layer (e.g., Al_2O_3 layer) on the metal surface usually plays a vital role in metal anti-corrosion, as it prevents the internal fresh metal from contacting with the external active reaction medium. For this matter, the honeycomb-like zinc surface acts as porous networks for the penetration of electrolyte inside and leads to accelerated corrosion behavior of the zinc foil and a deepened Zn corrosion layer. In order to reveal the formation mechanism of the honeycomb-like Zn surface, in-situ ultraviolet-visible (UV-vis) spectroscopy was conducted to record the changes in polyiodide concentration by soaking the zinc foil in polyiodide solution. As the absorbances at ~288 and

6

354 nm in UV-vis spectrum are highlighted as typical responses of I_3^-, they undergo a significant decline as function of time (Figure 1e).[27] This observation is absent in the blank control experiment without Zn foil in polyiodide solution (Figure S1, Supporting Information), confirming the spontaneous reaction between I_3^- ions and zinc under ambient conditions. Noteworthily, the intensity of another peak at ~225 nm that comes from the I^- ions shows a rising tendency with the decrease of the I_3^- concentration (Figure S2, Supporting Information), which demonstrates a spontaneous pathway occurring between I_3^- and Zn as the following equation (1).

$$Zn + I_3^- \rightarrow Zn^{2+} + I^- \tag{1}$$

Meanwhile, the honeycomb-like zinc foil (Figure 1c) is generated due to the gradual dissolution of the produced water-soluble ZnI_2 compound in the electrolyte solution. In order to match the battery situation better, symmetric Zn‖Zn cells were assembled to investigate the effect of polyiodide corrosion on Zn dendrite growth in different electrolytes, before which the symmetric cells were set for 3 days firstly. As shown in Figure 1f, the symmetric cell with the mixed electrolyte (composed of 90 vol% 2 M $ZnSO_4$ and 10 vol% aforementioned polyiodide solution) displays an extremely short life span (~5 h) at a current density of 1 mA cm^{-2}, while the cell using 2 M $ZnSO_4$ can work over 45 h at the same current density. Apparently, the corrosion behavior produced by polyiodide on a zinc surface greatly promotes dendrite growth and causes the cells to fail quickly. Notably, this result is inconsistent with previous studies,[28] which considered that polyiodide can inhibit dendrite growth. This may be due to their neglect of the corrosion of the electrodes caused by polyiodide during the battery's resting period. Therefore, the necessary measures should be taken to inhibit the corrosion of polyiodide towards zinc.

Summarizing, the effect of polyiodide on the Zn anode can be assigned to three processes as illustrated in Figure 1g with the details as follows: 1) the shuttled polyiodide will contact with the Zn anode and react to form water-soluble ZnI_2 firstly; 2) given that water-soluble

ZnI$_2$ dissolve into the electrolyte, the Zn foil will form a honeycomb and rugged structure gradually, which will lead to further passivation behavior occurring in the inner fresh zinc due to polyiodide and water corrosion; 3) owing to this deep ultra-irregular structure, the dendrite growth on the Zn surface will be extremely rampant and result in rapid battery failure ultimately. Therefore, an effective protective layer for the Zn anode is needed that serves multiple purposes in the Zn-I$_2$ system, i.e., providing uniform Zn plating/striping and keeping the Zn anode away from escaped polyiodide.
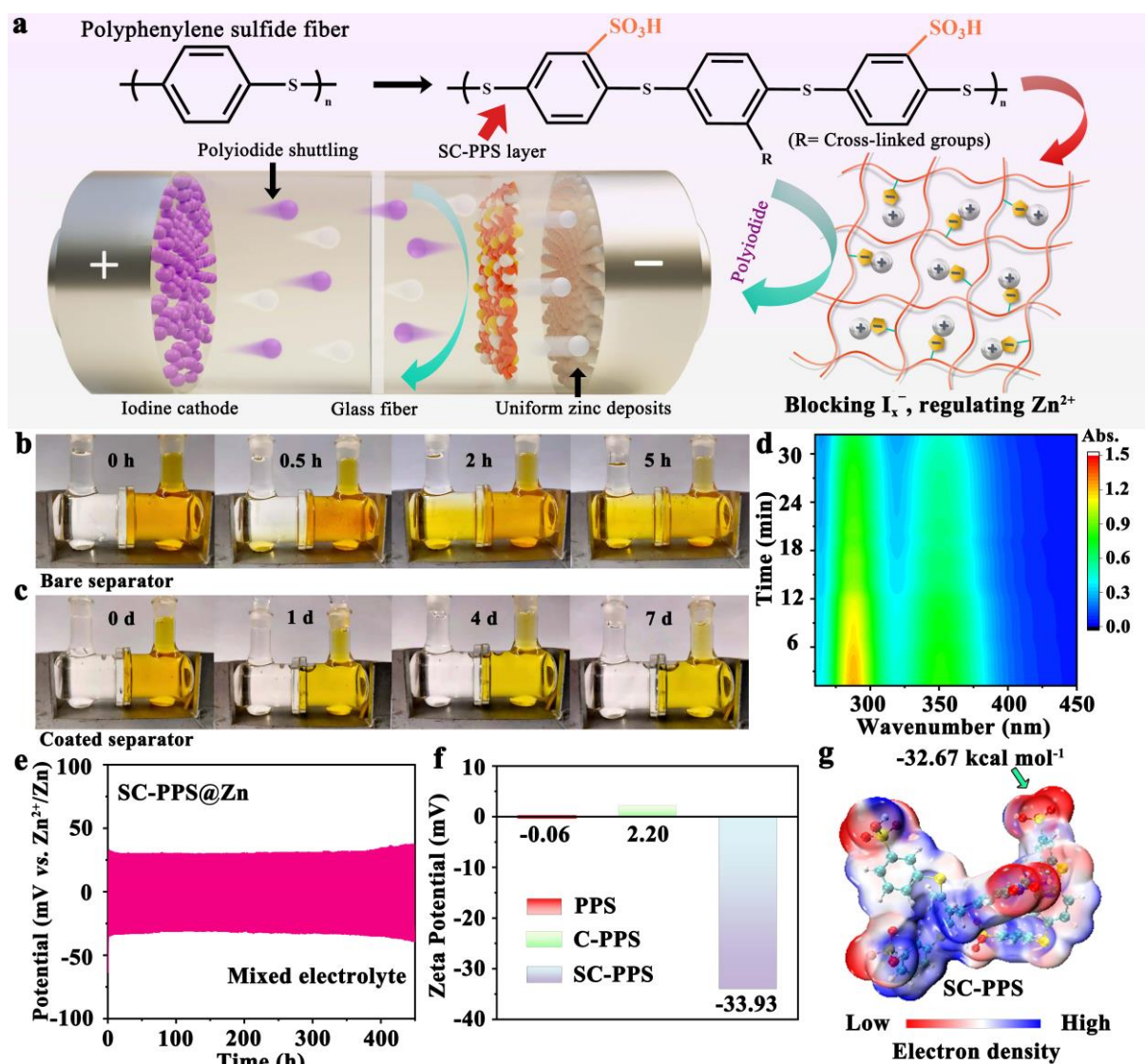

Figure 2. a) Schematic illustration for the brief synthesis process of SC-PPS, as well as its roles in realizing high-performance ZIBs. Optical images of H-type cells with aqueous polyiodide solution (the yellow region) using b) bare PP-separator, and c)

SC-PPS@PP-separator after setting for different times. d) In-situ UV-vis spectrum of aqueous polyiodide solution with SC-PPS@Zn. e) Electrochemical cycling behavior of a symmetric SC-PPS@Zn cell with the mixed electrolyte at a current density of 1 mA cm^{-2} (1 mAh cm^{-2}). f) Zeta potential values of PPS, C-PPS, and SC-PPS. g) Electrostatic potential distribution of SC-PPS.

As mentioned earlier, ion-exchange materials have the potential of alleviating the thorny issues faced by zinc-iodine battery anodes in theory, as they can rapidly achieve enrichment and separation of various ions in aqueous environments. A multifunctional polymeric coating with commercial polyphenylene sulfide (PPS) fiber skeletons and sulfonic acid functional groups (noted as SC-PPS), was engineered firstly by employing ion-exchange technology (**Figure 2**a). The as-developed SC-PPS coating is expected to block the shuttling polyiodide and to regulate the plating/stripping behavior of zinc ions through its favorable structural robustness and abundant active functional groups, leading to durable, green, and low-cost Zn-I$_2$ batteries. The building-up route of SC-PPS is summarized in Figure S3 (Supporting Information) with the detailed synthetic procedure in the experimental section. In brief, to avoid the self-condensation of p-xylylene dichloride, 1,4-bis(chloromethyl)-2-nitrobenzene (BCM-NB) was synthesized via the nitration reaction of p-xylylene dichloride.[29,30] In view of this, PPS can be directly cross-linked with BCM-NB via a Friedel-Crafts reaction (the resulting product is denoted as C-PPS), thereby inheriting of the toughness and insolubility of PPS fibers. Subsequently, the ion-exchange material of SC-PPS can be obtained by a simple sulfonation reaction of C-PPS using chlorosulfonic acid as the sulfonating agent. The photograph presented in Figure S4 (Supporting Information) shows the synthesis of SC-PPS in tens of grams (~16 g), reflecting the great commercialization potential of the developed SC-PPS coating.

The successful preparation of BCM-NB cross-linker was confirmed by Gas chromatography-mass spectrometery (GC-MS) in Figure S5 and S6 (Supporting Information), in which BCM-NB is the dominant product (89.21%) during the first-step reaction with a small amount of 1,4-bis(chloromethyl)-2,5-dinitrobenzene (6.93%) formed. As the 1,4-bis(chloromethyl)-2,5-dinitrobenzene even has an enhanced inhibitory effect on the self-condensation of p-xylylene dichloride (due to the introduction of the more electron-withdrawing $-NO_2$ groups), the subsequent complicated separation and purification of BCM-NB can be avoided. Furthermore, Fourier transform infrared spectroscopy (FTIR) was used to elucidate the chemical structure of the targeted polymers (Figure S7, Supporting Information). As compared with the fresh PPS, the FTIR spectrum of the C-PPS shows new peaks at ~1300 and ~1626 cm^{-1}, which correspond to the symmetric and antisymmetric stretching vibrations of nitryl group, respectively, indicating the success of cross-linking reaction. After the sulfonation of C-PSS, the peak appearing at 1169 cm^{-1} can be attributed to the asymmetric stretching vibration of SO_2-OH in the sulfonic acid group,[31] which demonstrates that the successful introduction of sulfonic acid groups into the SC-PPS. The X-ray photoelectron spectroscopy (XPS) results provided in Figure S8 (Supporting Information) further demonstrates the successful preparation of SC-PPS.

The influence of the thickness of the SC-PPS layer for the transport of polyiodide and Zn^{2+} ion is first investigated in Figure S9 (Supporting Information). Significantly, the battery resistance increases rapidly when the thickness of SC-PSS layer exceeds 100 μm, suggesting that an excessive thickness of coating will greatly retard the migration of Zn^{2+}. On the other hand, the permeation time of an ultrahigh concentration of polyiodide in an H-type cell rises systematically. Given comprehensive consideration, an SC-PPS layer with a thickness of 100 μm was chosen for the following research due to its high Zn^{2+} flux and sluggish polyiodide transport. The blockage effect of SC-PPS towards polyiodide was visualized in Figure 2b and

2c, where the polyiodide solution and blank solvent were separated by polypropylene (PP) and SC-PPS coated polypropylene (SC-PPS@PP) separators in H-type cells, respectively. With a pristine PP separator, the cell witnesses a distinct polyiodide diffusion process. Already after 5 h, the color of blank chamber changes from colorless to orange rapidly. By stark contrast, the as-prepared SC-PPS@PP separator enables the blank chamber to remain colorless for over 7 days, reflecting its great capability for blocking polyiodide diffusion. Furthermore, the excellent polyiodide obstruction of SC-PPS also suggests that a SC-PPS coating can protect Zn from polyiodide corrosion effectively, which was further demonstrated by the in-situ UV-vis spectroscopy. With the immersion of SC-PPS-coated Zn (SC-PPS@Zn) in polyiodide solution, the concentration of polyiodide hardly changes after setting for over 30 min (Figure 2d). Significantly, the corresponding cross-sectional morphology of Zn foil in Figure S10 (Supporting Information) presents a negligible corrosion layer. Moreover, the symmetric cell using SC-PPS@Zn foil is capable of working properly in polyiodide electrolyte over 400 h (Figure 2e), which is much longer than that of using bare Zn foil (5 h, Figure 1f). These results confirm that with our strategy, we have greatly prevented polyiodide from contacting the Zn anode and avoided undesired reactions between polyiodide and Zn, thus realizing in a highly stable Zn anode.

In get deeper insight in the obstruction ability of SC-PPS for polyiodide, a zeta potential measurement, that reflects the surface charge of the material, was performed. As shown in Figure 2f, SC-PPS shows the most negative zeta potential of -33.93 mV as compared to those of PPS (-0.06 mV) and C-PPS (2.20 mV), which demonstrates that the introduced sulfonic acid groups in SC-PPS should be of importance in inhibiting polyiodide shuttling by electrostatic repulsion. On the other hand, the electrostatic potential distribution and geometrically stable configuration of simulated SC-PPS chains are shown in Figure 2g and Figure S11 (Supporting Information), respectively. The sulfonic group in the SC-PPS chain

exhibits the largest electron density up to -32.67 kal mol^{-1} (red color region). Taken together, experiments and theory alike prove that the SC-PPS can block diffusion of polyiodide through electrostatic repulsion.
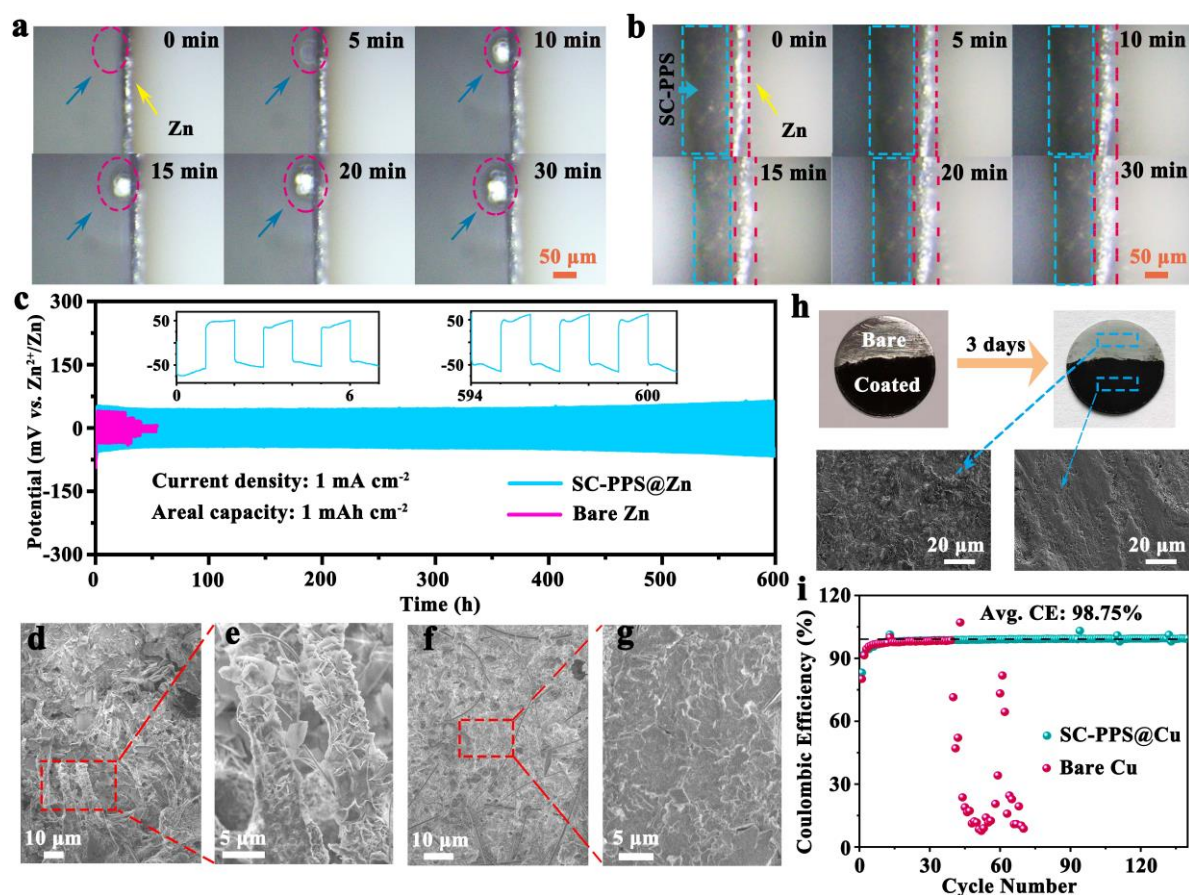

Figure 3. In-situ OM images of Zn deposits on a) bare Zn foil, and b) SC-PPS@Zn in a symmetric Zn cell with a current density of 0.5 mA cm^{-2}. c) Long-term galvanostatic cycle performance of symmetric Zn cells using bare Zn foil and SC-PPS@Zn at a current density of 1 mA cm^{-2} (1 mAh cm^{-2}). Insets are the detailed voltage profiles of a cell with the SC-PPS@Zn electrode at 1st cycle (left) and 300th cycle (right). SEM images of d),e) bare Zn foil, and f),g) SC-PPS@Zn (the SC-PPS layer was torn off) in symmetric Zn cells after 100 cycles at a current density of 1 mA cm^{-2}. h) The morphology of Zn plate with or without SC-PPS coating before and after being immersed in deionized water for 3 days. i) CE of Zn plating/stripping on SC-PPS@Cu/bare Cu foil at a current density of 0.5 mA cm^{-2} (0.5 mAh cm^{-2}) with a cut-voltage of 1.0 V.

1

Apart from polyiodide corrosion, the zinc anode is also frequently plagued by dendrite growth that mainly originates from the nonuniform contact between the electrolyte and Zn anode surface. To observe the effect of SC-PPS coating in regulating Zn plating/striping visually, in-situ OM was employed to monitor Zn deposition behavior at a current density of 0.5 mA cm^{-2}. Apparently, the Zn deposition on the bare Zn foil is uneven, with white Zn spots appearing after working for only 5 min (**Figure 3**a). As the deposition time increases, the size of Zn spot grows at a visible rate with a lateral width of ~56 μm at a deposition time of 30 min. On the contrary, SC-PPS@Zn shows a uniform deposition behavior during the whole plating process without detecting any visible Zn dendrites (Figure 3b). Simultaneously, a rapid horizontal growth of zinc foil is also observed, suggesting that SC-PSS layer allows the transport of Zn^{2+} ions to Zn surface instead of being deposited on the SC-PPS@Zn surface. As a result, the unwanted side reactions occurring at the interface of the freshly deposited Zn and electrolyte can be effectively avoided. Subsequently, the practical advantage of SC-PSS coating layer was evaluated by long-term galvanostatic cycling using the symmetric Zn cell. As shown in Figure 3c, the polarization voltage of the cell with bare Zn continues to decline irreversibly after working for 27 h at a current density of 1 mA cm^{-2} (1 mAh cm^{-2}). As the accumulation of detrimental by-products, the cell shuts down after 41 h. The cell with SC-PPS@Zn exhibits an ultra-long cycling life of over 600 h. The voltage curves after 600 h show a slight increase of ~10 mV as compared to that of the first cycle (insets of Figure 3c), demonstrating that an extremely reversible plating/stripping process can be well realized on the Zn anode with the SC-PSS layer. Moreover, when the current density increased from 1 mA cm^{-2} to 2 mA cm^{-2} (2 mAh cm^{-2}), the SC-PPS@Zn cell can still keep stable over 200 h (Figure S12, Supporting Information). The morphology of Zn deposition with or without SC-PSS coating was further investigated by SEM after 100 cycles at 0.5 mA cm^{-2} (0.5 mAh cm^{-2}). As shown in Figure 3d and 3e, the bare Zn exhibits a rugged surface consisting of

1

chaotic clusters and spiculate dendrites, which lead to rapid battery failure. In contrast, the deposition morphology obtained from the SC-PSS@Zn foil presents a compact, smooth, and dendrite-free surface (Figure 3f and 3g), demonstrating the formation of a reliable protective layer on the Zn surface, which is capable of greatly prolonging the lifetime of zinc anode. Notably, the SC-PSS coating also makes the zinc foil resistant to water corrosion. We immersed Zn foils with or without SC-PPS coating in deionized water for 3 days. As shown in Figure 3h, it is clear that the Zn foil with SC-PPS coating presents a smoother surface as compared to the bare one that has distinct particles and chunks on the surface. Owning to regulated zinc plating/stripping process and inhibited water corrosion, the Coulombic efficiency (CE) of a Zn||Cu coin-type cell with SC-PPS coating therefore shows excellent electrochemical performance. As demonstrated in Figure 3i, in stark contrast to the rapid battery failure observed on a bare Cu substrate, the coated Cu electrode (SC-PPS@Cu) manifests a high level of reversibility over 140 cycles with an average CE of 98.75%. Besides, the voltage-capacity curves for Zn deposition on the bare Cu and SC-PPS@Cu were provided in Figure S13 (Supporting Information). As compared with the rapid fluctuations on the bare Cu, the curves of SC-PPS@Cu almost overlap even after 50 cycles, reflecting the improved stability of SC-PPS coating to zinc stripping/deposition behavior. In view of this, it can be considered that a highly stable Zn anode can be realized by the tailor-made SC-PPS coating layer.
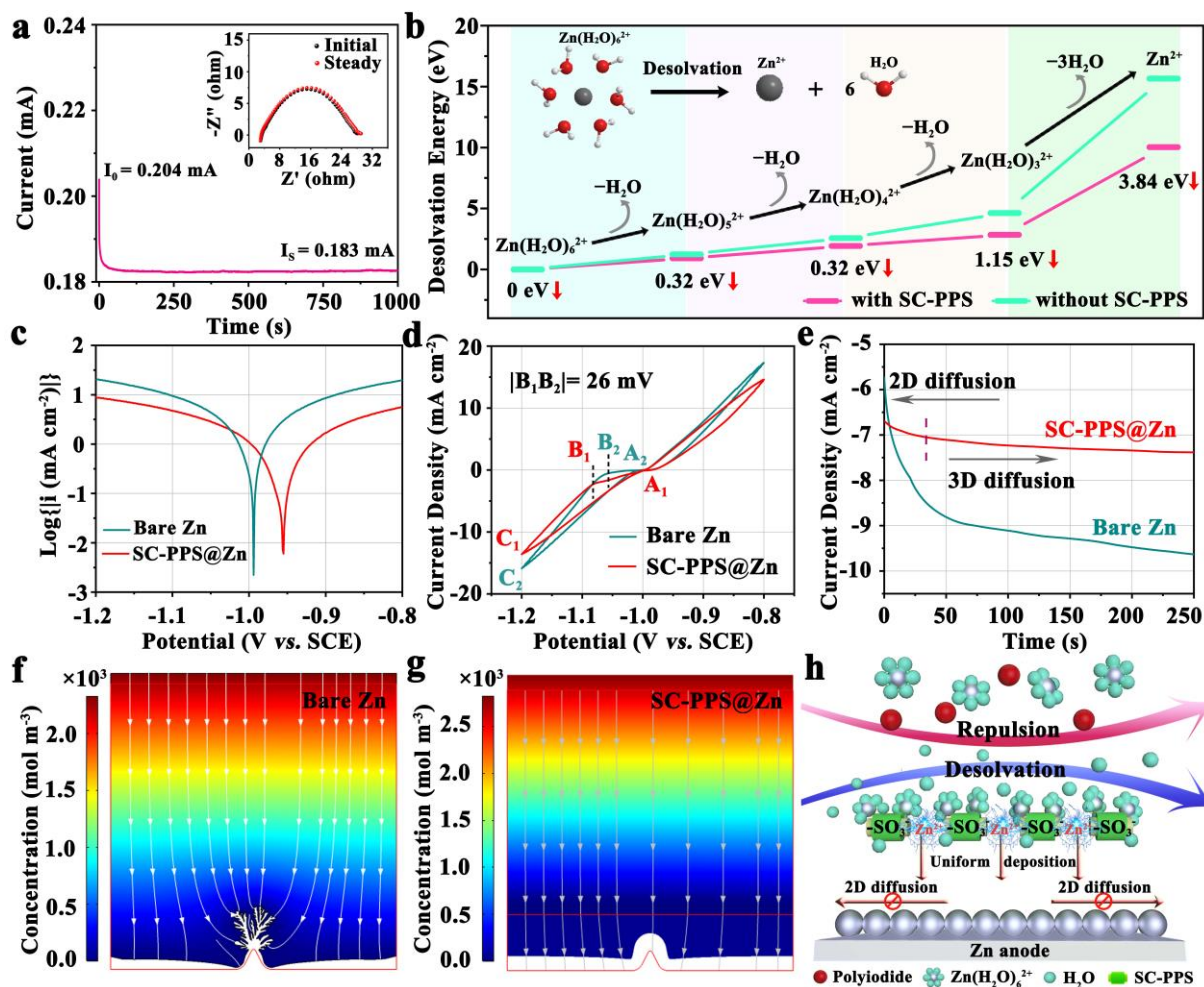
Figure 4. Investigation on the working mechanism of SC-PPC in realizing a highly stable of Zn anode. a) CA curve and the corresponding EIS plots of the symmetric cell. b) Desolvation energy values for the removal of H_2O molecules on $Zn(H_2O)_6^{2+}$ group with or without SC-PPS. c) Linear polarization curves showing the corrosion on bare Zn and SC-PPS@Zn. d) CV curves of bare Zn and SC-PPS@Zn with a scan rate of 0.1 mV s^{-1}. e) CA curves of bare Zn and SC-PPS@Zn at an overpotential of 150 mV. The growth of dendrites on f) bare Zn, and g) SC-PPS@Zn by COMSOL Multiphysics simulations at 100 s. h) Schematic illustration of the stabilization of Zn anode with SC-PPS layer.

We further elaborate on the underlying mechanism of SC-PPS coating in protecting the Zn anode from dendrites formation, as well as other possible side reactions. In general, the formation of zinc dendrites is caused by the lack of regulation for Zn^{2+} deposition. Firstly, SC-PPS was immersed into a 1 M ZnSO$_4$ solution to observe the influence of SC-PPS on Zn^{2+}.

1

As the SEM image and corresponding elemental mapping images shown in Figure S14 (Supporting Information), a uniform Zn-rich layer can be constructed on the SC-PPS surface that is expected to influence the growth and evolution of Zn dendrites during cycling. The content of Zn^{2+} ions in the immersed SC-PPS is also checked by chemical titration (the corresponding details can be obtained in the Supporting Information), which shows that each gram of SC-PPS can load about 0.79 mmol of Zn^{2+}. In view of this, the ionic conductivity (σ) as well as Zn^{2+} transference number (t_{Zn2+}) of SC-PPS coating can be evaluated based on the followed equations.[32]

$$\sigma = \frac{L}{AR} \tag{2}$$

$$t_{Zn^{2+}} = \frac{I_S(\Delta V - R_0)}{I_0(\Delta V - R_S)} \tag{3}$$

where R is impedance, L is the thickness of coating, A is the area of SC-PPS coating, ΔV is the voltage polarization applied, and I_0 (I_S) and R_0 (R_S) are the initial (steady) state current and resistance, respectively. As provided in **Figure 4**a, the σ and t_{Zn2+} of SC-PPS are 0.39 mS cm^{-1} and 0.82, respectively, which are significantly higher than those of commercial anion exchange membranes (σ: 0.27 mS cm^{-1}; t_{Zn2+}: 0.19).[33,34] As a whole, the sulfonate-rich interface of SC-PPS can not only modulate the Zn^{2+} flux by constructing a rich-Zn layer but also achieve efficient Zn^{2+} conduction.

On the other hand, it is well-known that each Zn^{2+} can coordinate with six H_2O molecules in $ZnSO_4$ electrolyte. However, free water molecules formed during the desolvation of Zn^{2+} could severely compromise the stability of Zn anode. Notably, the rich sulfonic acid groups in SC-PPS also affect the desolvation of Zn^{2+}. As revealed by the density functional theory (DFT) calculations in Figure 4b, the $Zn(H_2O)_6^{2+}$ group on the bare Zn foil requires high desolvation energies to remove different amounts of water molecules ($Zn(H_2O)_6^{2+} \rightarrow Zn(H_2O)_5^{2+}$: 1.24 eV; $Zn(H_2O)_5^{2+} \rightarrow Zn(H_2O)_4^{2+}$: 1.33 eV; $Zn(H_2O)_4^{2+} \rightarrow Zn(H_2O)_3^{2+}$: 2.06 eV; $Zn(H_2O)_3^{2+} \rightarrow Zn^{2+}$: 11.03 eV). However, given that each sulfonic acid group in SC-PPS is able to coordinate with

three H_2O molecules maximally (Figure S15, Supporting Information), the desolvation energies of $Zn(H_2O)_6^{2+}$ group decrease sharply with the application of SC-PPS layer ($Zn(H_2O)_6^{2+} \rightarrow Zn(H_2O)_5^{2+}$: 0.92 eV; $Zn(H_2O)_5^{2+} \rightarrow Zn(H_2O)_4^{2+}$: 1.01 eV; $Zn(H_2O)_4^{2+} \rightarrow Zn(H_2O)_3^{2+}$: 0.91 eV; $Zn(H_2O)_3^{2+} \rightarrow Zn^{2+}$: 7.19 eV), which demonstrates that the SC-PPS layer is beneficial to facilitating the desolvation of $Zn(H_2O)_6^{2+}$ group and forming Zn^{2+} ions. As a result, the amount of free water at the zinc/electrolyte interface will be reduced effectively, which would greatly mitigate the corresponding parasitic reaction caused by water on the Zn surface (e.g., H_2 evolution and dissolved O_2-induced passivation).[35] Besides, the facile desolvation process of Zn^{2+} is also expected to be the key to ameliorate the competitive reaction between Zn^{2+} and H^+ at the electrode-electrolyte interface.[36] Therefore, the DFT calculation provides a theoretical underpinning for the experimental observation of smooth Zn surface with SC-PPS coating and high CE of 98.75% in Figure 3h and 3i, which is further demonstrated by the linear polarization experiments in Figure 4c. The SC-PPS@Zn shows a more positive potential of −0.955 V as compared to the bare Zn foil (−0.994 V). Significantly, a more positive corrosion potential represents a reduced tendency for corrosion reaction.[37-39] To this end, the anti-corrosion capability of SC-PPS is attributed to the fact that the sulfonic acid groups can bond with free water and facilitate the desolvation of $Zn(H_2O)_6^{2+}$ groups. Besides, the introduction of PVDF into SC-PPS appears to reduce the hydrophilicity of the SC-PPS layer (Figure S16, Supporting Information), while a hydrophobic layer could enhance the corrosion resistance of zinc towards aqueous electrolytes.[40-42]

The interfacial environment between the SC-PPS@Zn electrode and $ZnSO_4$ electrolyte was further analyzed by conducting cyclic voltammetry (CV) tests in a three-electrode system. As plotted in Figure 4d, the point located at the intersection of nucleation processes is well-known as the crossover potential (E_{co}). The potential difference between the crossover point (A_1, A_2) and the point (B_1, B_2) is regarded as the nucleation overpotential (NOP), which

is usually employed as a parameter to evaluate the degree of polarization as well as the effect of electrode modification.[39,43] In particular, the relationship between the Zn^{2+} nucleation radius (r_{crit}) and NOP can be shown by the following relation.[44]

$$r_{crit} = 2\frac{\gamma V_m}{F|\eta|} \tag{4}$$

where γ is the surface energy of the Zn/electrolyte interface, V_m is the molar volume of Zn, F is Faraday's constant, and η is the NOP. Obviously, r_{crit} is inversely related to the value of NOP; the higher the NOP is, the smaller the grain size of Zn deposits becomes. Whereas fine-grained Zn deposits usually make a positive contribution to avoiding Zn dendrite growth. Experimentally, the SC-PPS@Zn presents a higher NOP of 82 mV than the bare Zn (56 mV), which is mainly derived from the strong interaction between Zn^{2+} ions (or partially hydrated Zn^{2+} ions) and sulfonic acid groups in SC-PSS layer. The increased NOP value can provide a sufficient driving force for the Zn nucleation and growth processes with finer nuclei. Besides, owing to the formation of zinc-rich adsorption layer on the Zn surface (Figure S14, Supporting Information), the flux of interfacial Zn^{2+} and the migration of Zn^{2+} species can be regulated effectively, causing uniform growth of Zn in subsequent stages.[45,46] Chronoamperometry (CA) analysis was further performed to examine the growth mechanism of the deposited films, as it is a typical method that can report on the changes in surface structure and in the nucleation process.[47-49] As shown in Figure 4e, for the bare Zn foil, the current density increases continuously even after 250 s under an overpotential of 150 mV. Normally, the absorbed metal ions first spread laterally along the surface and tend to deposit in an area where crystals already exist to lower the surface energy.[21,50] Therefore, the CA curve of bare Zn foil suggests that a rampant two-dimensional (2D) diffusion and rough deposition occur in the process of Zn^{2+} electrodeposition, leading to the rapid growth of Zn dendrite in Figure 3a. In stark contrast, the initial Zn nucleation and 2D diffusion process on the SC-PPS@Zn electrode last only for ~36 s with a flat plateau at a current density of ~7.2

1

mA cm^{-2}, which is closely related to a 3D diffusion process and indicates that the Zn^{2+} ions absorbed on the surface appear to be reduced to Zn^0 directly due to the constrained 2D surface diffusion.[39] Especially, this could be attributed to the strongly adhered sulfonic acid group to the Zn^{2+}, which provides an additional energy barrier (high NOP value) for the absorbed ions to move laterally. As a result, the Zn^{2+} ions are thus restricted to deposit near the initial adsorption sites on the Zn surface, and this leads to an even and dense Zn layer ultimately, as our observation in Figure 3b.

By far, the effect of SC-PPS coating on the electrodeposition of Zn^{2+} ions can be attributed to the accelerated Zn^{2+} transfer from the electrolyte to Zn anode and inhibited 2D diffusion of Zn^{2+} at the electrode/electrolyte interface by increasing NOP value. Bearing these in mind, we employed COMSOL Multiphysics to further simulate the dendrite growth on Zn foil with or without SC-PPS coating. As displayed in Figure S17 (Supporting Information), we firstly endow an initial protrusion on the Zn anode to represent its uneven surface. In this case, Zn^{2+} ions preferentially deposit at the protrusion to minimize the exposed area and surface energy when there is no SC-PPS coating, resulting in the rapid evolution of the protrusion into snowflake dendrite (Figure 4f). In particular, the Zn deposit (white section) is thin in the middle but thick on both sides, which will inevitably lead to further aggravation of dendrite growth. However, these adverse circumstances can be greatly improved after introducing the SC-PPS coating (the area surrounded by the red box in Figure 4g), as it accelerates Zn^{2+} transfer and inhibits the adverse 2D diffusion of Zn^{2+}. Significantly, the growth of Zn deposited layer exhibits an overall forward trend with the evolution of dendrites also being effectively suppressed. Therefore, both the COMSOL simulations and experimental results (Figure 3a and 3b) jointly suggest that the SC-PPS coating can regulate the deposition behavior of Zn^{2+} well and result in the generation of the dendrite-free Zn anode.

Overall, the mechanism by which the SC-PPS inhibits polyiodide shuttling, side reactions, and dendrite growth can be described as an outside-in process, as shown in Figure 4h. Depending on the electrostatic repulsion produced by the electronegative sulfonic acid groups, the SC-PPS can effectively prevent the polyiodide shuttle from contacting the Zn anode and avoid the corresponding parasitic reaction. Meanwhile, the hydrophilic sulfonic acid groups in SC-PPS are able to bond with free water and facilitate the desolvation of Zn^{2+}, which can mitigate the water corrosion and other side reactions effectively. In addition, the strong interaction between the sulfonic acid groups and Zn^{2+} can form a uniform Zn-rich coating on the Zn surface to inhibit the harmful 2D diffusion, thereby leading to the generation of an even and dense Zn layer.
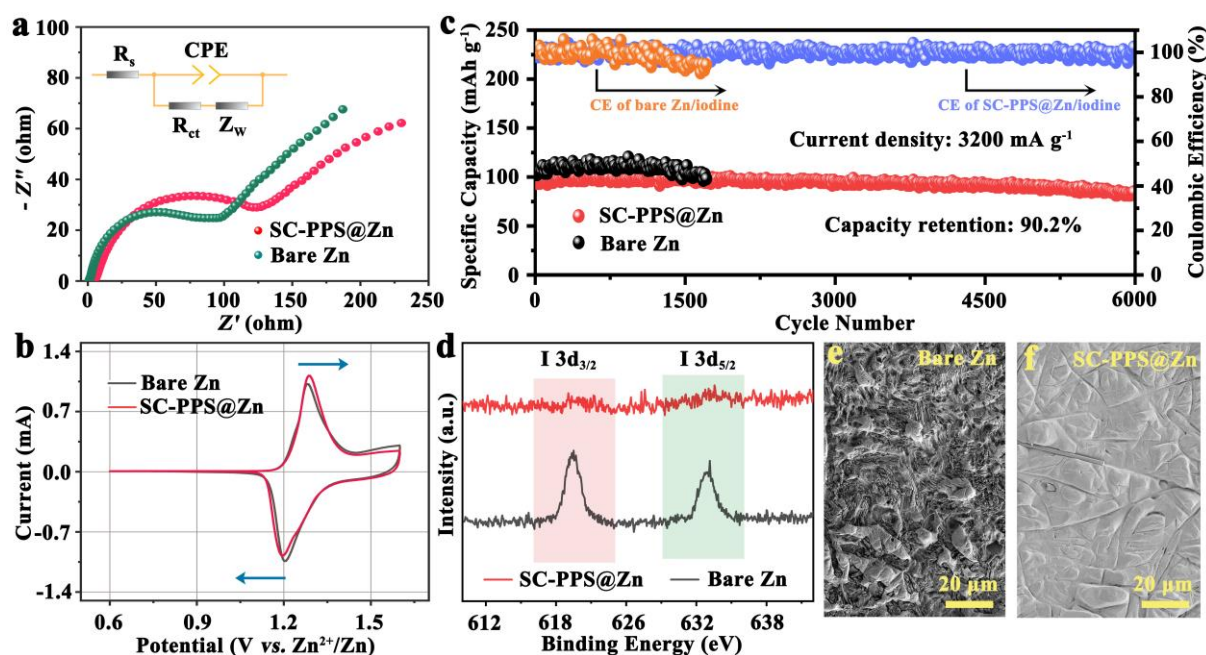

Figure 5. a) Comparison of the EIS spectra of Zn-I_2 cells with SC-PPS@Zn and bare Zn. b) CV profiles of Zn-I_2 cells with SC-PPS@Zn and bare Zn at a scan rate of 0.1 mV s^{-1}. c) Long-term cycling performance of Zn-I_2 cells at a current density of 3.2 A g^{-1}. d) Comparison of XPS spectra of Zn-I_2 cells with SC-PPS@Zn (the SC-PPS layer was torn off) and bare Zn after 1000 cycles. SEM images for the surface of e) bare Zn plate anode and f) SC-PPS@Zn after 1000 cycles.

2

The practical application of our strategy was further checked by assembling full Zn-I_2 coin-cells, where the cathode was prepared *via* the method reported in our previous work.[51] Electrochemical impedance spectroscopy (EIS) was conducted to evaluate the kinetics in Zn-I_2 cells. The corresponding equivalent circuit and fitting results for the Zn-I_2 cells are depicted in **Figure 5**a, where R_s stands for the purely ohmic resistance, the CPE is the constant phase element, the R_{ct} represents the charge transfer resistance, and the Z_W is related to the Warburg impedance.[52] The cell with the SC-PSS layer shows a slightly larger charge-transfer resistance of ~120 Ω than that of the cell with bare Zn (~100 Ω), which is apparently associated with the SC-PSS layer-induced overpotential. An identical conclusion can also be deduced from the cyclic voltammetry (CV) profiles (Figure 5b), where the polarization potential of the cell with SC-PPS@Zn (~93 mV) is slightly increased as compared to that of bare Zn (~79 mV). As for the long-term cycling performance of the cells evaluated in Figure 5c, the cell with SC-PPS coating can operate stably over 6000 cycles corresponding to a capacity retention of 90.2% and an average CE up to 99.89% with a reversible capacity of 84.6 mAh g^{-1} (current density: 3.2 A g^{-1}). Comparatively, Zn-I_2 batteries with the bare Zn anode exhibit a short-life span (~1700 cycles) due to the dendrite growth and polyiodide corrosion. To further corroborate this, the Zn-I_2 cells were disassembled after 1000 cycles and the as-obtained Zn anodes were checked by XPS technique. As shown in Figure 5d, the signal corresponding to iodine species is clearly visible on the bare Zn due to the shuttle effect of polyiodide. This means that Zn anode will encounter the direct attack of polyiodide. Nevertheless, iodine species on the coated Zn (the SC-PPS layer was torn off) show an ignorable signal, indicating that SC-PPS coating can protect zinc anode from polyiodide corrosion. Hence, it comes as no surprise that the SEM image of Zn anode with the SC-PPS coating remains dense and dendrite-free surface, while the bare Zn shows a rough and chaotic surface (Figure 5e). The rate performance of Zn-I_2 cell

with the SC-PPS@Zn anode was also evaluated. As depicted in Figure S18 (Supporting Information), the specific capacity of battery is capable of reaching up to 93.8 mAh g^{-1} under a high current density of 20 C, corresponding to ~72% (130.4 mAh g^{-1}) at 1 C. In particular, after reversing the applied currents back to 1, 2, 5, 10, and 20 C successively, the reversible capacities of battery can be almost recovered. Figure S19 (Supporting Information) also shows the corresponding charge-discharge voltage profiles of the cell, in which the discharge platform is mainly above ~1.1 V, fully reflecting the advantage of Zn-I$_2$ battery against the counterparts with intercalation/de-intercalation mechanisms. Moreover, we also employed the active carbon/I$_2$ cathode to evaluate the performance of the SC-PPS layer. As shown in Figure S20 (Supporting Information), the Zn-I$_2$ cell with the SC-PPS@Zn anode can maintain an ultra-high capacity with ~100% retention after 1500 cycles compared to cell with bare zinc anode (~94.2% after 1500 cycles). When applying the carbon paper as the cathode (by adding 0.1 M KI as the iodine source), the battery with the SC-PSS@Zn anode is able to maintain a specific capacity of ~40 mAh g^{-1} after 1000 cycles (Figure S21a, Supporting Information). While the battery without SC-PSS coating cannot be recharged (Figure S21b, Supporting Information). These results fully confirm the intriguing potential of the as-developed SC-PSS coating layer in the pursuit of low-cost, practically viable, and durable Zn-I$_2$ batteries.

3. Conclusion

In summary, we have identified that the corrosion of polyiodide on Zn anode is an important contributing factor to the short-life span of zinc-iodine batteries. The construction of a sulfonated 1,4-bis(chloromethyl)-2-nitrobenzene crosslinked polyphenylene sulfide (SC-PPS) ion-exchange layer on the Zn surface can effectively protect the Zn anode from polyiodide due to the strong electrostatic repulsion generated by the abundant sulfonic acid groups in SC-PPS. Simultaneously, such a sulfonate-rich polymer coating can form a uniform rich-Zn layer on the Zn surface, which accelerates the transfer of Zn^{2+} and restrict the rough

two-dimension diffusion, thus realizing a homogeneous and dense Zn deposition. Besides, this coating also shows resistance to water corrosion, as the sulfonic acid groups can bond with free water and facilitate the desolvation of Zn^{2+}, significantly reducing the damage of free water to the anode. Consequently, zinc-iodine batteries with a SC-PPS coating can operate stably over 6000 cycles while maintaining a high capacity retention of 90.2% and an average Coulombic efficiency up to 99.89%. This work not only systematically analyzed the adverse effect of polyiodide on Zn anode, but also provided a high operability solution to develop long-life, low-cost, and intrinsic safety aqueous zinc-iodine batteries.

4. Experimental Section

Materials and chemicals: Dichloroethane (99%), $ZnSO_4$ (99%), *p*-xylylene dichloride (98%), aluminium trichloride anhydrous (99%), and *N*-methyl-2-pyrrolidinone (NMP, 99.5%) were purchased from Shanghai Aladdin Biochemical Technology Co., Ltd. Nitrobenzene (99%, Shanghai Yien Chemical Technology Co., Ltd), chlorosulfonic acid (99%, Saen Chemical Technology Co., Ltd), and polyphenylene sulfide fiber (PPS, Sichuan Deyang Technology Co., Ltd) were purchased from different technology firms. The PPS was washed with deionized water and ethanol before being used, while all other reagents were used as received without further purification.

Synthesis of 1,4-bis(chloromethyl)-2-nitrobenzene (BCM-NB): 4.20 g of *p*-xylylene dichloride was dissolved into 39 mL of dichloroethane and stirred in an ice bath, followed by dropwise addition of mixed acid (composed of 65% nitric acid (2.51 mL) and 98% sulfuric acid (13.70 mL)) through the constant pressure dripping funnel. Reaction mixture was heated to 60 °C for 5 h and subsequently cooled down to 0 °C. The BCM-NB was obtained by washing with deionized water until became neutral.

Synthesis of 1,4-bis(chloromethyl)-2-nitrobenzene crosslinked polyphenylene sulfide (C-PPS): 6.41 g of aluminium trichloride anhydrous was dissolved in 666 mL of dichloroethane and 40 mL of nitrobenzene. Subsequently, the as-obtained BCM-NB and 12.96 g of polyphenylene sulfide fiber was added into the mixed solution, and heated to 80 °C for 24 h under N_2 atmosphere. The C-PPS was obtained by washing with ethanol, and vacuum-drying at 60 °C for 24 h.

Synthesis of sulfonated 1,4-bis(chloromethyl)-2-nitrobenzene crosslinked polyphenylene sulfide (SC-PPS): 15.24 mL of chlorosulfonic acid was firstly added into 687 mL of dichloroethane. Then, 14.00 g of C-PPS fiber was added into the mixed solution, and heated to 80 °C for 3 h. The SC-PPS can be obtained by washing with deionized water, and vacuum-drying at 60 °C for 24 h.

Synthesis of *N,N′*-dimethyl-1,3-propanediamine-grafted, and triethylenetetramine-crosslinked acrylic fiber/iodide (GC-PAN/I): GC-PAN/I was synthesized by the method that we reported previously.[51] In short, 1.0 g of acrylic fiber was grafted with 35.7 g of *N,N′*-dimethyl-1,3-propanediamine, and crosslinked with 1.7 g of triethylenetetramine at 135 °C under reflux for 12 h. Whereafter, the product was washed with deionized water and ethanol, and then vacuum-dried at 60 °C for 12 h. Next, 1.0 g of product was immersed in 22.2 g of *N,N′*-dimethylformamide, and then 1.4 g of methyl iodide was added into the solution. The reaction mixture was heated to 40 °C under reflux and kept for 8 h. The resultant SC-PPS can be obtained by washing with deionized water and ethanol.

Materials and structural characterizations: The scanning electron microscopy (SEM) was performed to characterize the morphology of the samples based on COXEM EM-30 PLUS. The Fourier transform infrared spectroscopy (FTIR, Bruker Tewsor) and X-ray photoelectron spectroscopy (XPS, AXIS Supra) were conducted to check the chemical structures of samples. Ultraviolet-visible spectroscopy (UV-vis) analyses were used to determine the change in iodine concentration by Shimadzu UV-2450 spectrometer. Zeta potential analyses of materials were performed on Litesizer 500.

Electrochemical characterizations: The SC-PPS (85%) was mixed with polyvinylidene difluoride (10%) and Super P (5%), in which the Super P acts as a grinding aid. The as-prepared slurries were coated onto Zn foil (thickness: 0.3 mm) using *N*-methyl-2-pyrrolidone as the solvent. After vacuum-drying at 45 °C for 24 h, the coated anode can be obtained. The cathode was prepared through the same procedure, while the GC-PAN/I, polyvinylidene difluoride, and Super P were mixed in a mass ratio of 8:1:1. The CR2032-type coin cells were assembled in an open atmosphere using 2 M $ZnSO_4$ as the electrolyte with a sandwich structure (Zn anode, glass fiber membrane, and GC-PAN/I cathode). Three-electrode system was prepared with saturated calomel electrode (SCE) as the reference electrode, Zn/coated Zn (0.03 mm) as the working electrode, and graphite rod as the counter-electrode. Active mass loadings of anode and cathode are 3−4 mg cm^{-2} and 1−2 mg cm^{-2}, respectively. Both the specific capacity of the battery and the applied current density are

2

calculated based on the mass of iodine. Long-term cycling performance of the cell was conducted on a LAND-CT2001A system. Cyclic voltammetry (CV), electrochemical impedance spectrum (EIS), and chronoamperometry (CA) were carried out on CHI660E electrochemical test station.

Chemical titration experiments: 0.5440 g of fiber was firstly immersed in 100 mL of 0.25 M $ZnSO_4$ solution for 12 h at 30 °C in a constant temperature incubator shaker. After filtering the fiber, three solutions (each of 20 mL) were obtained. Then, the concentration of Zn^{2+} in the solution was determined by chemical titration with ethylene diamine tetraacetic acid standard solution (0.1 mol L^{-1}) as the titrant and xylenol orange as the indicator. Therefore, the content of zinc ions adsorbed by SC-PPS (0.79 mmol g^{-1}) can be calculated through the concentration difference before and after adsorption.

Density functional theory (DFT) calculations: All quantum chemical calculations, including geometry optimizations and single-point energy calculations, were performed at the PBE1PBE[53]/def2svp[54,55] level with the D3 version of Grimme's dispersion with Becke-Johnson damping[56] in the quantum chemical package Gaussian 09[57]. The electrostatic potential distribution mapping of SC-PPS was obtained by Visual Molecular Dynamics and Multiwfn treatment.[58-60]

COMSOL Multiphysics simulations: As shown in Figure S17, a two-dimensional Zn symmetric cell model was established based on COMSOL Multiphysics software. Then, the "Tertiary current distribution" interface was selected to describe the current and potential distributions in the cell and analyze the transport of Zn ions species in the electrolyte, while Butler-Volmer expression was further used to reveal the electrode kinetics of the charge transfer reaction at room temperature in the bulk electrolyte. Besides, we further used deformation geometry to track the changes of Zn anode boundary during electroplating.

Supporting Information

Supporting Information is available from the Wiley Online Library or from the author.

Acknowledgements

Conflict of Interest

The authors declare no conflict of interest.

References

[1] E. C. Evarts, *Nature* **2015**, *526*, S93.

[2] W. Du, E. H. Ang, Y. Yang, Y. Zhang, M. Ye, C. C. Li, *Energy Environ. Sci.* **2020**, *13*, 3330.

[3] J. B. Goodenough, *Nat. Electron.* **2018**, *1*, 204.

[4] W. Zong, N. Chui, Z. Tian, Y. Li, C. Yang, D. Rao, W. Wang, J. Huang, J. Wang, F. Lai, T. Liu, *Adv. Sci.* **2021**, *8*, 2004142.

[5] J. Liu, W. Zhou, R. Zhao, Z. Yang, W. Li, D. Chao, S.-Z. Qiao, D. Zhao, *J. Am. Chem. Soc.* **2021**, *143*, 15475.

[6] Z. Yang, B. Wang, Y. Chen, W. Zhou, H. Li, R. Zhao, X. Li, T. Zhang, F. Bu, Z. Zhao, W. Li, D. Chao, D. Zhao, *Natl. Sci. Rev.* **2022**, DOI: 10.1093/nsr/nwac268.

[7] H. Yang, Y. Qiao, Z. Chang, H. Deng, P. He, H. Zhou, *Adv. Mater.* **2020**, *32*, e2004240.

[8] P. A. Lyday, in Ullmann's Encyclopedia of Industrial Chemistry, WileyVCH, Weinheim, Germany **2000**.

[9] Y. Zou, T. Liu, Q. Du, Y. Li, H. Yi, X. Zhou, Z. Li, L. Gao, L. Zhang, X. Liang, *Nat. Commun.* **2021**, *12*, 170.

[10] L. Ma, Y. Ying, S. Chen, Z. Huang, X. Li, H. Huang, C. Zhi, *Angew. Chem. Int. Ed.* **2021**, *60*, 3791-3798; *Angew. Chem.* **2021**, *133*, 3835.

[11] Z. Wang, M. Zhou, L. Qin, M. Chen, Z. Chen, S. Guo, L. Wang, G. Fang, S. Liang, *eScience* **2022**, *2*, 209.

[12] X. Li, N. Li, Z. Huang, Z. Chen, G. Liang, Q. Yang, M. Li, Y. Zhao, L. Ma, B. Dong, Q. Huang, J. Fan, C. Zhi, *Adv. Mater.* **2021**, *33*, e2006897.

[13] D. Lin, Y. Li, *Adv.Mater.* **2022,** *34*, 2108856.

[14] S. Yang, X. Guo, H. Lv, C. Han, A. Chen, Z. Tang, X. Li, C. Zhi, H. Li, *ACS Nano* **2022**, *16*, 13554.

[15] L. Yan, S. Zhang, Q. Kang, X. Meng, Z. Li, T. Liu, T. Ma, Z. Lin, *Energy Storage Mater.* **2023**, *54*, 339.

[16] K. Lu, H. Zhang, B. Song, W. Pan, H. Ma, J. Zhang, *Electrochim. Acta* **2019**, *296*, 755.

[17] X. Zeng, X. Meng, W. Jiang, J. Liu, M. Ling, L. Yan, C. Liang, *ACS Sustainable Chem. Eng.* **2020**, *8*, 14280.

[18] H. Li, C. Guo, T. Zhang, P. Xue, R. Zhao, W. Zhou, W. Li, A. Elzatahry, D. Zhao, D. Chao, *Nano Lett.* **2022**, *22*, 4223.

[19] Z. Hou, T. Zhang, X. Liu, Z. Xu, J. Liu, W. Zhou, Y. Qian, H. J. Fan, D. Chao, D. Zhao *Sci. Adv.* **2022**, *8*, eabp8960.

[20] B. Tang, L. Shan, S. Liang, J. Zhou. *Energy Environ. Sci.* **2019**, *12*, 3288.

[21] C. Li, X. Xie, S. Liang, J. Zhou, *Energy Environ. Mater.* **2020**, *3*, 146.

[22] J. Zheng, D. C. Bock, T. Tang, Q. Zhao, J. Yin, K. R. Tallman, G. Wheeler, X. Liu, Y. Deng, S. Jin, A. C. Marschilok, E. S. Takeuchi, K. J. Takeuchi, L. A. Archer, *Nature Energy* **2021**, *6*, 398.

[23] R. Chen, Q. Yang, Y. Zhong, X. Li, Y. Liu, X.-M. Li, W.-X. Du, G.-M. Zeng, *Desalination* **2014**, *344*, 306.

[24] X. Li, H. Zhang, Z. Mai, H. Zhang, I. Vankelecom, *Energy Environ. Sci.* **2011**, *4*, 1147.

[25] E. Ramírez, R. Soto, R. Bringué, M. Iborra, J. Tejero, *Ind. Eng. Chem. Res.* **2020**, *59*, 20676.

[26] S. Bolisetty, M. Peydayesh, R. Mezzenga, *Chem. Soc. Rev.* **2019**, *48*, 463.

[27] Y.-J. Wei, C.-G. Liu, L.-P. Mo, *Spectrosc. Spect. Anal.* **2005**, *25*, 86.

[28] S. Liu, W. Shang, Y. Yang, D. Kang, C. Li, B. Sun, L. Kang, S. Yun, F. Jiang, *Batteries Supercaps* **2022**, *5*, e202100221.

[29] C. D. Wood, B. Tan, A. Trewin, H. Niu, D. Bradshaw, M. J. Rosseinsky, Y. Z. Khimyak, N. L. Campbell, R. Kirk, E. Stöckel, A. I. Cooper, *Chem. Mater.* **2007**, *19*, 2034.

[30] M. P. Tsyurupa , V. A. Davankov, *React. Funct. Polym.* **2002**, *53*, 193.

[31] N. Zwettler, J. S. Engbæk, R. Lundsgaard, I. Paranowska, T. E. Nielsen, S. Clyens, J. Christiansen, M. Ø. Andersen, *React. Funct. Polym.* **2015**, *88*, 47.

[32] C. Liu, J. Wang, W. Kou, Z. Yang, P. Zhai, Y. Liu, W. Wu, J. Wang, *Chem. Eng. J.* **2021**, *404*, 126517.

[33] Y. Yuan, J. Yang, Z. Liu, R. Tan, M. Chuai, J. Sun, Y. Xu, X. Zheng, M. Wang, T. Ahmad, *Adv. Energy Mater.* **2022**, *12*, 2103705.

[34] L. Cao, D. Li, T. Pollard, T. Deng, B. Zhang, C. Yang, L. Chen, J. Vatamanu, E. Hu, M. J. Hourwitz, *Nat. Nanotechnol.* **2021**, *16*, 902.

[35] Y. Cui, Q. Zhao, X. Wu, X. Chen, J. Yang, Y. Wang, R. Qin, S. Ding, Y. Song, J. Wu, K. Yang, Z. Wang, Z. Mei, Z. Song, H. Wu, Z. Jiang, G. Qian, L. Yang, F. Pan, *Angew. Chem. Int. Ed.* **2020**, *59*, 16594; *Angew. Chem.* **2020**, *132*, 16737.

[36] L. E. Blanc, D. Kundu, L. F. Nazar, *Joule* **2020**, *4*, 771.

[37] M. Abdel-All, Z. Ahmed, M. Hassan, *J. Appl. Electrochem.* **1992**, *22*, 1104.

[38] M. Abdallah, *Corros. Sci.* **2003**, *45*, 2705.

[39] Z. Zhao, J. Zhao, Z. Hu, J. Li, J. Li, Y. Zhang, C. Wang, G. Cui, *Energy Environ. Sci.* **2019**, *12*, 1938.

[40] Z. Tao, Y. Zhu, Z. Zhou, A. Wang, Y. Tan, Z. Chen, M. Yu, Ya. Yang, *Small* **2022**, *18*, 2107971.

[41] Q. Wen, H. Fu, Z. Wang, Y. Huang, Z. He, C. Yan, J. Mao, K. Dai, X. Zhang, J. Zheng, *J. Mater. Chem. A* **2022**, *10*, 17501.

[42] K. Guan, L. Tao, R. Yang, H. Zhang, N. Wang, H. Wan, J. Cui, J. Zhang, H. Wang, H. Wang, *Adv. Energy Mater.* **2022**, *12*, 2103557.

[43] B. C. Tripathy, S. C. Das, G. T. Hefter, P. Singh. *J. Appl. Electrochem.* **1997**, *27*, 673.

[44] A. Pei, G. Zheng, F. Shi, Y. Li, Y. Cui, *Nano Lett.* **2017**, *17*, 1132.

[45] Z. Hong, V. Viswanathan. *ACS Energy Lett.* **2019**, *4*, 1012.

[46] G. Garcia, E. Ventosa, W. Schuhmann, *ACS Appl. Mater. Interfaces* **2017**, *9*, 18691.

[47] J. W. Diggle, A. Damjanovic, *J. Electrochem. Soc.* **1972**, *119*, 1649.

[48] R. Wang, D. Kirk, G. Zhang, *J. Electrochem. Soc.* **2006**, *153*, C357.

[49] J. Wang, L. Zhang, C. Zhang, J. Zhang, *J. Power Sources* **2001**, *102*, 139.

[50] G. Trejo, H. Ruiz, R. O. Borges, Y. Meas, *J. Appl. Electrochem.* **2001**, *31*, 685.

[51] L. Zhang, M. Zhang, H. Guo, Z. Tian, L. Ge, G. He, J. Huang, J. Wang, T. Liu, I. P. Parkin, F. Lai, *Adv. Sci.* **2022**, *9*, 2105598.

[52] J. Huang, Y. Li, R. Xie, J. Li, Z. Tian, G. Chai, Y. Zhang, F. Lai, G. He, C. Liu, T. Liu, D. J.L. Brett, *J. Energy Chem.* **2021**, *58*, 147.

[53] C. Adamo, V. Barone, *J. Chem. Phys*. **1999**, *110*, 6158.

[54] F. Weigend, R. Ahlrichs, *Phys. Chem. Chem. Phys.* **2005**, *7*, 3297.

[55] F. Weigend, *Phys. Chem. Chem. Phys.* **2006**, *8*, 1057.

[56] S. Grimme, S. Ehrlich, L. Goerigk, *J. Comp. Chem.* **2011**, *32*, 1456.

[57] Gaussian 09, Revision D.01, M. J. Frisch, G. W. Trucks, H. B. Schlegel, G. E. Scuseria, M. A. Robb, J. R. Cheeseman, G. Scalmani, V. Barone, B. Mennucci, G. A. Petersson, H. Nakatsuji, M. Caricato, X. Li, H. P. Hratchian, A. F. Izmaylov, J. Bloino, G. Zheng, J. L. Sonnenberg, M. Hada, M. Ehara, K. Toyota, R. Fukuda, J. Hasegawa, M. Ishida, T. Nakajima, Y. Honda, O. Kitao, H. Nakai, T. Vreven, J. A. Montgomery, Jr., J. E. Peralta, F. Ogliaro, M. Bearpark, J. J. Heyd, E. Brothers, K. N. Kudin, V. N. Staroverov, T. Keith, R. Kobayashi, J. Normand, K. Raghavachari, A. Rendell, J. C. Burant, S. S. Iyengar, J. Tomasi, M. Cossi, N. Rega, J. M. Millam, M. Klene, J. E. Knox, J. B. Cross, V. Bakken, C. Adamo, J. Jaramillo, R. Gomperts, R. E. Stratmann, O. Yazyev, A. J. Austin, R. Cammi, C. Pomelli, J. W. Ochterski, R. L. Martin, K. Morokuma, V. G. Zakrzewski, G. A. Voth, P. Salvador, J. J. Dannenberg, S. Dapprich, A. D. Daniels, O. Farkas, J. B. Foresman, J. V. Ortiz, J. Cioslowski, and D. J. Fox, Gaussian, Inc., Wallingford CT, **2013**.

[58] W. Humphrey, A. Dalke, K. Schulten, *J. Molec. Graphics* **1996**, *14*, 33.

[59] T. Lu, F. Chen, *J. Mol. Graph. Model.* **2012**, *38*, 314.

[60] T. Lu, F. Chen, *J. Comput. Chem.* **2012**, *33*, 580.